DOI: 10.1002/ejic.201100017

Synthesis of Well-Dispersed Aqueous-Phase Magnetite Nanoparticles and Their Metabolism as an MRI Contrast Agent for the Reticuloendothelial System

Yujun Song,*[a] Ruixue Wang,[b][‡] Rong Rong,[c][‡] Jie Ding,[a][‡] Jing Liu,[c][‡] Runsheng Li,[a][‡] Zhenghua Liu,[c] Hao Li,[a] Xiaoying Wang,*[c] Jue Zhang,*[b] and Jing Fang[b]

Keywords: Nanoparticles / Magnetite / Aqueous phase / Metabolism / Magnetic resonance imaging / Magnetic properties / Reticuloendothelial system

Aqueous-phase Fe_3O_4 nanoparticles (NPs), with a size of 9.8 ± 3.0 nm, are directly synthesized by a modified iron salt coprecipitation process, stabilized by the synergistic effect of a combination of poly(vinylpyrrolidone) (PVP), trisodium citrate (TSC), and maleic anhydride (MAH). These NPs show good aqueous-phase dispersion stability and excellent superparamagnetic properties with a saturation magnetization of 48.0 emu/g at a low magnetic field of 0.5 T. Their biocompatibility and metabolism for application in magnetic resonance reticuloendothelial system examinations are investigated by using rabbits as animal models for the determination of optimized dosage and diagnosis time for the enhanced imaging contrast for the early diagnosis of diseases. Results indicate that a significant darkening effect on the liver epithelial net lymph tissue can be observed in less than 30 min, with about 20 % reduction of the spin–spin relaxation time of T_2 after injection. A metabolism study on the NPs indicates that they show little toxicity to the living organs examined, and finally enter into the spleen without obvious retention in any related organs after recycling for more than 2 d.

Introduction

Over recent decades,[1–5] superparamagnetic NPs have been intensively investigated as magnetic resonance (MR) T_1 and T_2/T_2* spin–spin relaxation contrast agents. Various clinical and new imaging applications have been developed for these NPs, including the imaging of reticule endothelial systems such as the liver and spleen, perfusion imaging of the brain and brain tumors, myocardium and kidney, MR angiography, tumor vascular imaging, improved tumor delineration, imaging of thrombus, detection of lymph node metastases, magnetically labeled cell probe imaging, and tracking of cell migration.[1–4] Although some have been commercialized (e.g. Feridex, γ-Fe_2O_3), new NPs (e.g. Fe_3O_4, CoFe, $MnFe_2O_4$) are in development for their enhanced magnetic properties and stability, which can be used to provide a high signal-to-noise ratio at lower dosages.[5]

Recent research has focused on creating customized shapes and sizes of these new biocompatible species, which can be absorbed by human cellular structures for medical applications. For medical applications such as magnetic resonance imaging (MRI), magnetic drug targeting, hyperthermia, anticancer treatments, and enzyme immobilization, the effectiveness may rely on generating well-dispersed NPs with a narrow size distribution in aqueous solution.[5–7] Fe_3O_4 NPs have been most promising as new MRI contrast enhancers by greatly improving alternations of proton relaxation in the tissue environment at a low cost.[5] After serving their purposes in clinical diagnosis, these NPs can then be captured and disposed of by the liver without adverse effects.[5]

Various methods have been reported for the synthesis of Fe_3O_4 NPs, such as sol–gel techniques, reduction of hematite by H_2, coprecipitation from a solution of ferrous/ferric mixed salts, microemulsion methods, thermal decomposition of organometallic compounds, microwave hydrothermal synthesis, and microwave plasma synthesis.[6,8–11] These methods may be able to prepare magnetite with controllable particle sizes and shapes. Thermolysis of iron compounds in organic solvents at high temperatures has been well developed for monodispersed Fe_3O_4 NPs.[5,12,13] However tedious, the solvent replacement process has to be carried out

[a] Key Laboratory of Aerospace Materials and Performance (Ministry of Education), School of Materials Science and Engineering, Beihang University,
Beijing 100191, China
E-mail: songyj@buaa.edu.cn
[b] Academy for Advanced Interdisciplinary Studies,
Peking University,
Beijing 100871, China
E-mail: zhangjue365@yahoo.com.cn
[c] Department of Radiology, Peking University First Hospital,
Beijing 100034, China
E-mail: cjr.wangxiaoying@vip.163.com
[‡] These authors have contributed to the article equally
Supporting information for this article is available on the WWW under http://dx.doi.org/10.1002/ejic.201100017.

to transfer these organic-phase NPs into the aqueous phase, which usually results in size and shape variations and poor dispersion and stability.[5,6,12,14] To date, direct synthesis of well-dispersed aqueous Fe_3O_4 nanoparticles on a large scale has met with very limited success. Success of large-scale synthesis is desired for economical clinical possibilities.

Chemical coprecipitation is a convenient and economical method that has the potential to meet the increasing demand for the direct preparation of well-dispersed Fe_3O_4 nanoparticles in the aqueous phase.[15–17] Chemical coprecipitation can produce ultrafine, high-purity, stoichiometric particles of single and multicomponent metal oxides. Furthermore, if the process conditions such as solution pH, reaction temperature, stirring rate, solute concentration, and surfactant concentration are carefully controlled, oxide particles of the desired shape and size can be produced.[18]

In the development of new contrast agents for the early clinical diagnosis of diseases, the metabolism of the NPs in the body is a primary factor in the determination of optimized dosage and diagnosis time for the highest contrast images as well as their biosafety. In this article, a modified mixed iron salt coprecipitation process has been developed for the synthesis of well-dispersed Fe_3O_4 NPs by using PVP as the dispersion agent with TSC and MAH as costabilizers. The resulting spinel magnetite nanoparticles, with a size of 9.8 ± 3.0 nm, exhibit good aqueous stability and excellent superparamagnetic properties. From the administration of these NPs into rabbits, the kinetics of the imaging contrast of MR T_2 relaxation in different organs was observed and recorded to examine the biocompatibility and response time of these NPs as MRI contrast agents. The histopathological slices of related organs at different recycling times are further investigated to identify the metabolism and cytotoxicity of these NPs in the living organism by using rabbits as animal models.

Results and Discussion

The synthesis of well-dispersed Fe_3O_4 nanoparticles with excellent aqueous stability is essential for their clinical application as MRI contrast agents. The mixed iron salt precipitation process has been developed for the synthesis of Fe_3O_4 NPs, whose dispersion and stability in solution depend on their surface coating agents (Scheme 1).[5,6]

PVP and TSC are good dispersion agents, well developed for NP synthesis by using a wet chemical process, due to their good biocompatibility and aqueous dispersing ability.[19–21] TSC has been used in the synthesis of water-soluble iron oxide (Fe_3O_4, Fe_2O_3) NPs.[22] Here we used them to synthesize well-dispersed aqueous stable Fe_3O_4 NPs. However, they were unable to produce well-dispersed Fe_3O_4 NPs with the desired stability. When only PVP or TSC is used as the dispersion agent, the NPs obtained settled out of solution in less than 1 d. When PVP and TSC are used in the reaction system together, the stability of the NPs is only slightly improved. This instability is probably caused by the magnetic attraction among the large NPs and the weak binding between these dispersion agents and the surface of the Fe_3O_4 NPs, which cannot prevent aggregation. Considering the stabilizing ability of multichelating agents and the surface chemical properties of Fe_3O_4 NPs,[6,22] hydrophilic MAH, with its two carboxylic acid groups, may improve the water stability of the NPs. However, it was

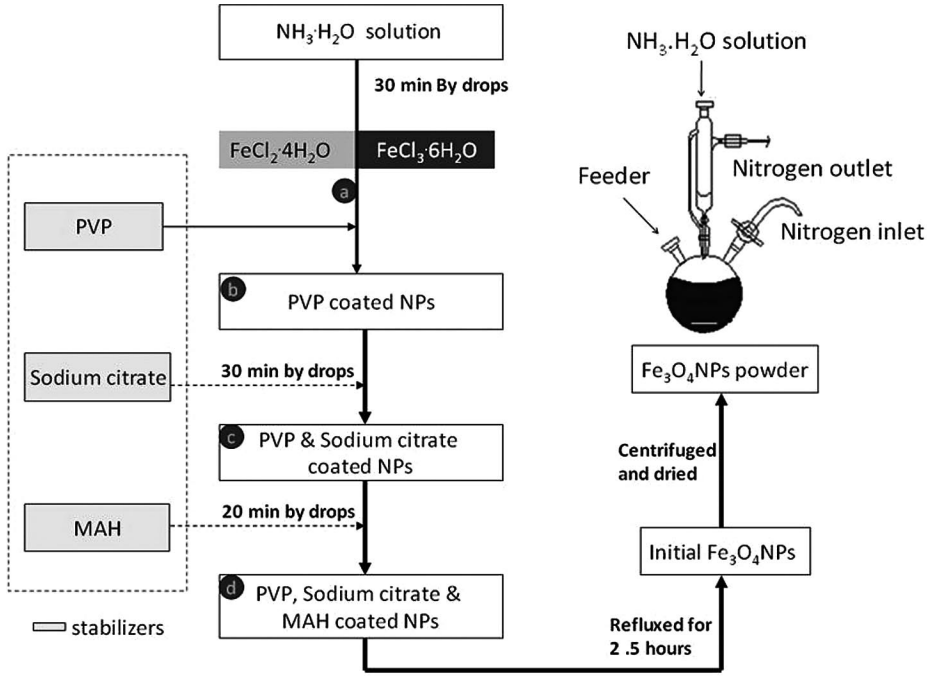

Scheme 1. Procedure for the preparation of Fe_3O_4 nanoparticles by a modified chemical coprecipitation method stabilized by the synergistic effect of PVP, TSC, and MAH.

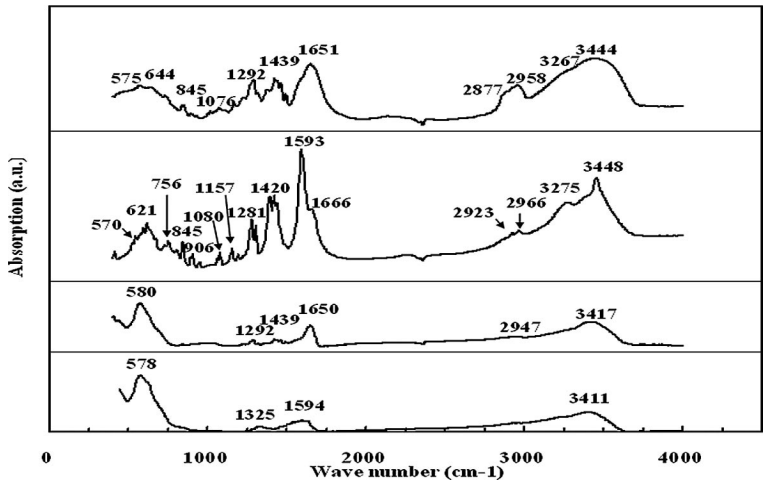

Figure 1. FTIR spectra of (a) standard bare Fe_3O_4, (b) Fe_3O_4 NPs coated with PVP, (c) Fe_3O_4 NPs coated with PVP and TSC, (d) Fe_3O_4 NPs coated with PVP, TSC, and MAH.

found that when only MAH was used, the stability was not greatly increased, probably due to its small molecular volume. Therefore, the three stabilizing agents were used together to test if they could increase the stability of the Fe_3O_4 NPs. The result shows that the stability of the formed NPs in water solution was greatly enhanced without any noticeable precipitation for at least four weeks. In order to examine the coating effect of MAH to the NPs, FTIR spectra of bare Fe_3O_4 NPs (a), Fe_3O_4 NPs coated with PVP (b), Fe_3O_4 NPs coated with PVP and TSC (c), and Fe_3O_4 NPs coated with PVP, TSC, and MAH were recorded and are summarized in Figure 1.

The FTIR absorption for the bare Fe_3O_4 shows features observed by other researchers, with characteristic peaks at around 578 and 3411 cm^{-1}, which can be assigned to the lattice absorption of the Fe–O bond vibration and the stretching vibrations of OH groups on the surface of the Fe_3O_4 NPs (Scheme 2A), respectively (Figure 1).[23,24] Some peak position and width shifts are observed in different samples, indicating the different binding effects of these stabilizers on the surface of the Fe_3O_4 NPs.[24–27] When using PVP as the dispersing agent (Figure 1b), some new absorption peaks typical for PVP appear besides the peaks from the Fe_3O_4 (a sharp peak at 580 cm^{-1} for Fe–O bonds and a broad peak at 3417 cm^{-1} for OH groups) (Figure 1a). The sharp peak at 1650 cm^{-1} is from C=O stretching in PVP, and the peak at 1292 cm^{-1} can be attributed to the stretching vibrations of the C–N bond in the amide group and the two other C–N groups.[23,28–30] Peaks appearing at 2947 and 1439 cm^{-1} can be attributed to the asymmetric stretching vibration and the scissoring bending vibration, respectively, of CH_2 groups in PVP.[23] Compared to the FTIR spectra for pure PVP (Figure S1) and bare Fe_3O_4, the peak shifts of the vibration bands of the carbonyl group, the vibrations of OH, and the suppressed vibrations at 2947, 1439, and 1292 cm^{-1} in the spectrum of the PVP-coated NPs suggest that PVP is modified on the surface of the Fe_3O_4 NPs by a coordination interaction through the C=O groups.[27] However, the similarity of these FTIR spectra in the 580–582 cm^{-1} region suggests that the coordination interaction through the carbonyl groups is not very strong. There are only some physical interactions (such as van der Walls forces) and/or hydrogen bonds between PVP and the Fe_3O_4 NPs. The redshift of the C=O stretch from 1682 cm^{-1} to 1651 cm^{-1} in PVP (Figure S1a) is probably either due to the reduced electron density from the interaction between the C=O bonds in PVP and the OH groups in the Fe_3O_4 NPs or the formation of hydrogen bonds between the C=O bonds and the OH groups, as shown in the stabilizing mechanism of the synergistic effect by the three compounds (Scheme 2B).

When TSC is added to the PVP-coated NPs (Figure 1c), the FTIR spectrum has obvious differences to that of the bare Fe_3O_4 and the PVP-dispersed Fe_3O_4 NPs. The typical peak for Fe–O vibration at about 578 cm^{-1} shifts to 621 cm^{-1} due to the enhanced electron density from the interaction of the COO^- groups in TSC and the Fe d orbital.[31] The interaction is suggested by the replacement of some OH groups in Fe_3O_4 NPs by COO^- groups from TSC (Scheme 2C). The two peaks at 1712 and 1757 cm^{-1} in pure TSC (Figure S1b) redshift to 1593 cm^{-1}, with enhanced intensity, and 1666 cm^{-1}, with suppressed intensity, in the NPs (Figure 1c), respectively, suggesting the formation of a complex between the carboxylate in TSC and the Fe_3O_4 NPs, as shown in the dashed circles in Scheme 2C; alternatively, an oxygen atom in TSC could exchange with an oxygen atom in Fe_3O_4 to form an Fe_3O_3OCO complex. Comparing the corresponding peaks in pure TSC and PVP (Figure S1b), variations in the peaks, the enhanced peaks at 1281 and 1420 cm^{-1}, and the suppressed peaks from 756–1157 cm^{-1} in the spectrum of the PVP–TSC-coated NPs can be interpreted by a coordination interaction between TSC, PVP, and Fe_3O_4.[23,28–30,32] Peaks at 1281 and 1420 cm^{-1} are due to stretching vibrations of C–O bonds and deformation vibrations of COH bonds in TSC,[33] respectively, which are increased in intensity by the interaction between TSC and Fe_3O_4 NPs and mixed with the peak at 1420 cm^{-1} due to the scissoring bending vibration of CH_2 groups and

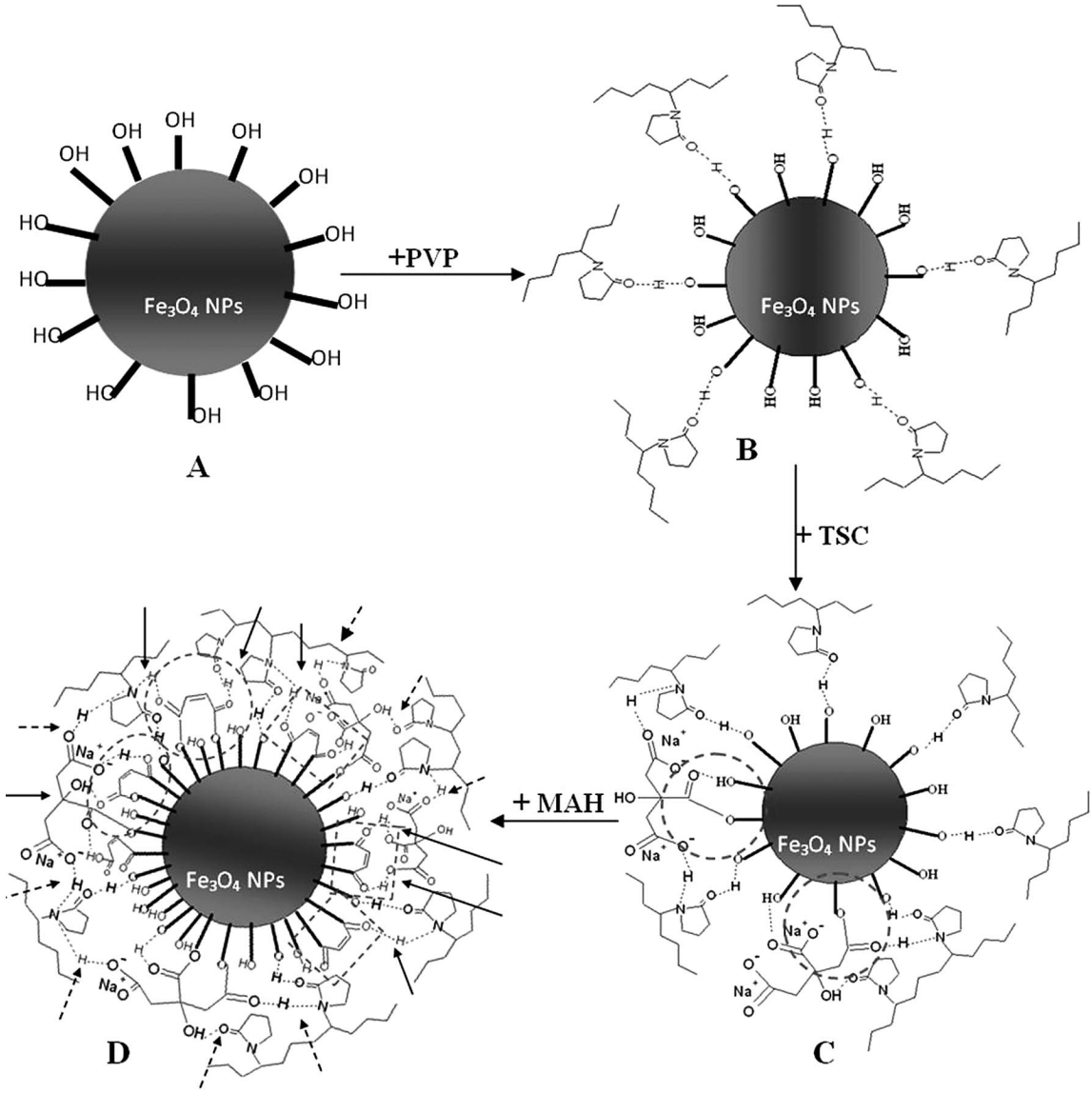

Scheme 2. Proposed synergistic stabilizing mechanism by the three compounds; (a) proposed bare Fe_3O_4 NPs coated with hydroxy groups, (b) proposed surface groups of PVP-coated Fe_3O_4 NPs, (c) proposed surface groups of PVP–TSC coated Fe_3O_4 NPs, (d) proposed surface groups of PVP–TSC–MAH coated Fe_3O_4 NPs.

1292 cm^{-1} for the stretching vibrations of the C–N bonds in PVP-coated Fe_3O_4 NPs. The low-intensity peak at 1081 cm^{-1} is attributed to the stretching vibration of C–C or C–O groups in TSC and the C–C backbone in the PVP.[33] The weak peak at 1157 cm^{-1} suggests that there are probably some C–O–C bonds formed in the PVP–TSC-stabilized Fe_3O_4 NPs.[33] These results indicate that some efficient coordination interactions between the stabilizers and the Fe_3O_4 NPs can be formed by the combination of PVP and TSC. Our experiment suggests that the stability of the Fe_3O_4 NPs coated by TSC and PVP is significantly increased, and these NPs are stable in their mother aqueous solution for 3–4 d. However, this does not satisfy the stability requirement for commercialized clinical testing of at least several months.

On the basis of the proposed stabilizing mechanism (Scheme 2) and the FTIR differences between the PVP-coated NPs and TSC–PVP-coated NPs, the enhanced aqueous stability for TSC–PVP-coated NPs is probably from the directed formation of Fe_3O_3OCO groups as well as the other coordination interactions (e.g. hydrogen bonds) between the stabilizers and the Fe_3O_4 NPs. Therefore, the stability can be further improved if more Fe_3O_3OCO complexes are formed. Considering this, MAH was added into the PVP- and TSC-coated NP solution, which gave an encouraging result. The Fe_3O_4 NPs formed show high aqueous stability, without any traceable aggregation and precipitation after leaving the solution undisturbed for at least four months. As indicated by significant differences between the FTIR spectra (Figure 1d), there is a strong interaction between the MAH and the NPs. After the addition of MAH, the peaks at 575–845, 1076, 1292, 1439, 1651, 2877–2958, and 3444 cm^{-1} are far broader, suggesting a strong synergistic effect between the three dispersion agents. The peak

at 574 cm^{-1} (Figure 1d) representing the Fe–O bonds in the NPs becomes broadened and splits into two peaks at 575 and 644 cm^{-1}. This broad peak also merges with that at 845 cm^{-1}, which represents the stretching vibration of CCO groups from MAH or TSC.[34] These results suggest that the Fe–O bond in the bare Fe_3O_4 becomes indistinct, meaning that the interface between the surface of the NPs and the stabilizers becomes unclear due to the MAH incorporation, or that strong bonds are formed among the NPs and stabilizers. The peak at about 1651 cm^{-1} (Figure 1d) becomes extremely strong and broad, merging the vibrations of C=O bonds from all of the stabilizers, indicating the formation of strong bonds between the carboxylate groups in the stabilizers and the Fe_3O_4 NPs after the addition of MAH.[32] By comparing the intensities and shapes of these peaks appearing in Figure 1, this complexation is mainly attributed to the strong chelating effect of the carboxylate group bonding to the Fe_3O_4 NP surfaces. There may be three main ways of chelating between MAH and Fe_3O_4 NPs during addition of MAH into the aqueous solution of NPs due to the hydrolysis of MAH. The strongest chelation can occur when both of the carboxylate groups in MAH coordinate to the Fe_3O_4 NPs, and the oxygen atoms in MAH exchange with the oxygen atoms in Fe_3O_4 before they hydrolyze into acids, as shown in the dashed squares in Scheme 2D. The second way of chelating can occur when only one carboxylate group in MAH coordinates to Fe_3O_4 and the other will coordinate with the OH group on the surface of the Fe_3O_4 NPs, as shown in the dashed ellipse in Scheme 2D. The weakest chelation may occur when both of the carboxylate groups in MAH coordinate with the OH groups on the surface of the Fe_3O_4 NPs, as shown in the dashed circle in Scheme 2D. The effect of MAH on the coordination between the stabilizers and the Fe_3O_4 NPs can be further evidenced by the peak at 1292 cm^{-1}, which is caused by enhanced C–N bonds in PVP, the C–O bonds in TSC and/or MAH by the interaction between the carboxylate groups in PVP, MAH, and TSC. This strong, broad peak indicates a strong interaction, most probably caused by the formation of hydrogen bonds between the stabilizers (see the arrows in Scheme 2D; dashed line: typical hydrogen bonds between TSC and PVP; solid line: typical hydrogen bonds between MAH and TSC or PVP). The broad peak at 1439 cm^{-1} can be ascribed to symmetric COO^- stretches from the combination of TSC and MAH.[24] The new broad peak at 1076 cm^{-1} represents the C=C bonds existing in MAH and/or the vibrations of C–C and C–O bonds from the TSC or PVP.[33] The broadened peak at 3444 cm^{-1} indicates that more OH groups exist in the coated Fe_3O_4 NPs after addition of MAH, endowing the Fe_3O_4 NPs with a higher hydrophilicity. The stronger peaks appearing from 2877 cm^{-1} to 2958 cm^{-1} in the NPs (Figure 1d) primarily result from the CH_2 asymmetric stretching and CH_3 symmetric stretching vibration of PVP and/or TSC being affected by MAH, which in turn shows a high interaction with the other stabilizers.

The Fe_3O_4 NPs stabilized only by the combination of PVP and MAH were also examined. Their stability was found to be similar to that of NPs stabilized by PVP alone, or by the combination of PVP and TSC. They do not show high aqueous stability, and the NPs settle in less than 3 d. Therefore, the high aqueous stability of the NPs stabilized by the combination of PVP, TSC, and MAH is clearly a result of a synergistic effect between the three stabilizers. Here, MAH can chelate with Fe_3O_4 by forming some strong bonds as an inner-layer stabilizer. TSC may provide the NPs with more COO^- groups to increase their hydrophilicity and/or modify the surface charge of NPs as the stabilizer in the middle layer. These NPs can be further dispersed and protected by the macromolecules of PVP as an outer layer, which prevents the NPs from approaching each other and aggregating. Enough hydrogen bonds formed between these stabilizers and the OH groups in Fe_3O_4 NPs will construct an efficient molecular interconnection surrounding the Fe_3O_4 NPs, which will significantly increase the stability of the Fe_3O_4 NPs in aqueous solution together with the strong chelating effect of MAH (Scheme 2D).

In order to further confirm that the stabilization is a result of synergistic effects between PVP, TSC, and MAH on the surface of the NPs, thermogravimetric analysis (TGA) measurements of the NPs were conducted to reveal if they were bound on the surfaces of the Fe_3O_4 NPs. As shown in Figure 2, the TGA data show four weight loss stages. The weight loss below 120 °C is due to removal of moisture (absorbed and bound water, approximately 7 wt.-%) from the sample. About 13 wt.-% weight loss in the second weight-loss stage from about 200 °C to 380 °C is due to the decomposition of TSC,[36] and about 37 wt.-% weight loss in the third weight-loss stage from 380 °C to 580 °C is caused by the decomposition of PVP.[35] It is known that maleic acid can become MAH by losing H_2O on heating. The MAH containing a double bond and an anhydride group can experience addition and condensation polymerization at elevated temperatures to form dimers (e.g. *exo*-7-oxabicyclo[2.2.1]hept-5-ene-2,3-dicarboxylic anhydride) and other condensed copolymers with high thermal stability.[37,38] Hence, it can be concluded that the fourth weight-loss stage is probably from the formed dimers or other condensed copolymers of MAH, which will decompose at a higher temperature than MAH, PVP, and TSC, and occupies about 15 wt.-%. Results from the TGA analysis suggest that the surfaces on the NPs are coated by the mixture of PVP, TSC, maleic acid, and the derivatives of maleic acids. Since the NPs undergo a thorough washing step, it can be concluded, from comparison of the amounts of each of the chemicals used in the reaction, that most of the TSC and the majority of PVP are washed out, and most of the MAH is bound to the surface of the NPs. If the amounts of these three chemicals added in the reaction solution are compared, it is obvious that the coating efficiency relative to the total amount of each chemical used follows the sequence of MAH > PVP > TSC. Although the FTIR results indicate that TSC may coordinate with Fe_3O_4 NPs more intensively than PVP, the whole chain of one PVP molecule may adhere to the surface of Fe_3O_4 NPs more tightly than one TSC molecule due to the many C=O groups in one PVP molecule (PVP mole-

cules are not shown in their entirety in Scheme 2B for simplicity). Thus, it can be deduced that most of the MAH and some of the PVP are tightly bound on the surface of the NPs, and only a small amount of the TSC is bound on top. Therefore, a greater amount of MAH can chelate to the surface of the NPs, compared to the amount PVP, and these are much larger amounts than that of TSC. However, the experimental results show that MAH cannot stabilize the NPs without PVP and TSC. The PVP and TSC attached on the surface of the NPs may play roles, such as creating steric hindrance and charge repulsion, which keep the NPs from aggregating. In addition, hydrogen bonds can be formed between MAH and TSC or PVP, which will further stabilize the NPs as shown in Scheme 2D. The TGA result gives additional evidence for the synergistic effect between the PVP, TSC, and MAH on the stabilization of these NPs. Further experiments are being performed to elucidate a detailed and more reasonable stabilizing mechanism based on the synergistic effect.

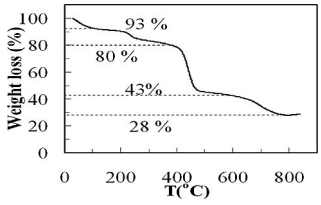

Figure 2. TGA curve of Fe_3O_4 NPs.

The synergistic effect of the three stabilizers gives the NPs good dispersion in aqueous solution as shown by their TEM images [Figure 3(a)], which show well-separated NPs with little aggregation. The size of the NPs, based on 472 NPs, is calculated as 9.8 ± 3.0 nm with a size standard deviation of about 31%, whose histogram is shown inset in Figure 3(a). The mass ratio of Fe/O in the NPs after thorough washing is measured as 2.62 by energy-dispersive X-ray analysis (EDS) [Figure 3(b)], which is almost the same as the stoichiometric Fe/O mass ratio in Fe_3O_4 (2.618). The selected-area electron diffraction (SAED) pattern for these NPs gives dotted rings [inset in Figure 3(c)], suggesting that these NPs have good crystallinity. Analysis of the *d*-spacing of these rings suggests that the dotted rings represent the Bragg reflections of [111], [220], [311], [400], [422], [511], and [440] crystal planes from the inner ring to the outer one [Figure 3(c)], giving the iron oxide NPs a standard face-centered cubic (fcc) spinel Fe_3O_4 crystal structure.[33,39] Diffraction from the [222] plane near to the strongest diffraction from the [311] plane cannot be clearly discerned in the SAED pattern due to the weak diffraction intensity and/or the merging effect from the nearby strong diffraction plane [311].[14,33,39] The high-resolution TEM (HRTEM) image for one typical single Fe_3O_4 NP [Figure 3(d)] confirms its perfect crystallinity by showing crystal lattice fringe spacings of around 4.72 Å and 2.83 Å, corresponding to the [111] and [220] lattice planes in cubic Fe_3O_4 NPs.[39] The SAED pattern [inset in Figure 3(d)] of this single Fe_3O_4 NP shows uniform bright diffractive dots, with the structure analysis being consistent with the result from its HRTEM image.

The XRD of the Fe_3O_4 NPs was recorded to further elucidate their crystal structure and to estimate their size. As shown in Figure 4, the XRD pattern indicates that these

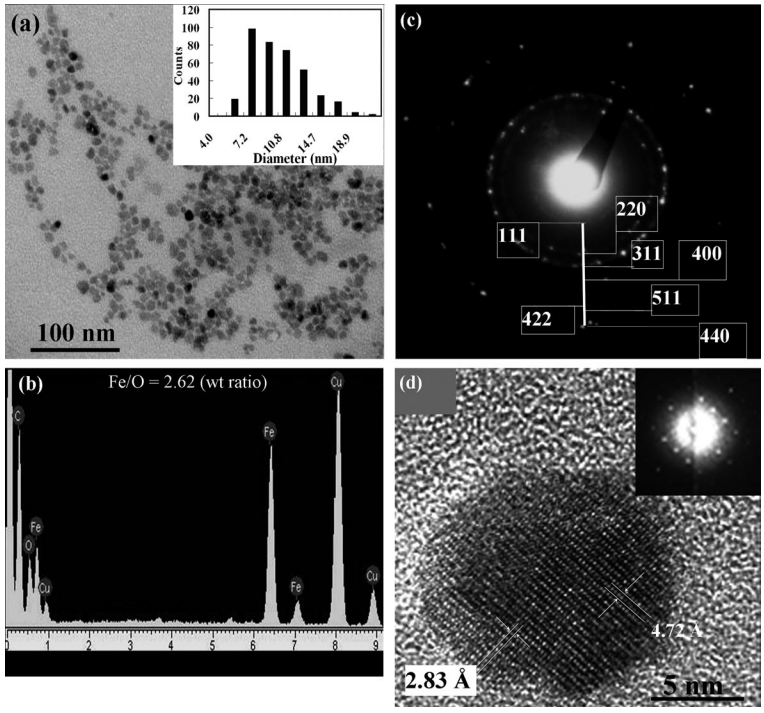

Figure 3. (a) Typical TEM image of the Fe_3O_4 NPs; the inset shows a histogram of the size distribution of Fe_3O_4 NPs (average diameter: 9.8 ± 3.0 nm), (b) EDS of Fe_3O_4 NPs, (c) electron-diffraction pattern of an ensemble of Fe_3O_4 NPs, (d) HRTEM image of a typical single crystal of Fe_3O_4 NPs with distinct crystalline lattices.

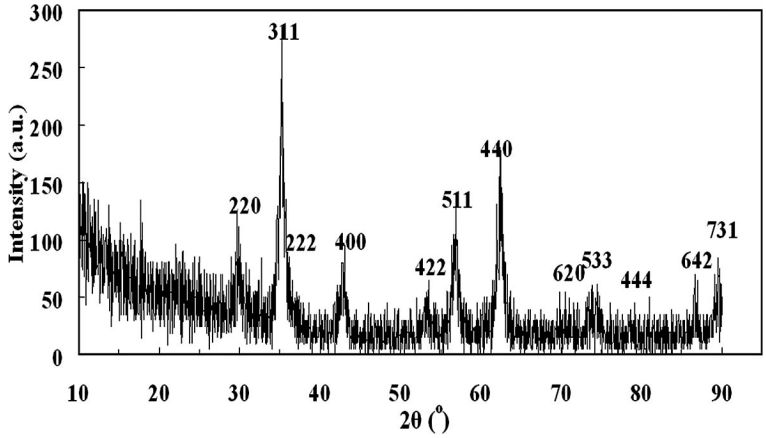

Figure 4. XRD characterization of the synthesized Fe_3O_4 NPs.

NPs preserve the typical features of the magnetite spinel phase, with a series of characteristic peaks at 2θ = 17.96, 29.85, 35.27, 37.16, 42.76, 53.36, 56.64, 62.47, 70.58, 74.34, 79.20, 86.60, and 89.86°, which correspond to [111], [220], [311], [222], [400], [422], [511], [440], [620], [533], [444], [642], and [731] Bragg reflections, respectively, agreeing with the standard magnetite (Fe_3O_4) XRD JCPDS file (PDF No. 79-0419) by comparison with other iron oxide compounds [$Fe(OH)_3$, hematite, maghemite, and goethite].[34,40] The *d*-spacing for [111], [220], [311], [400] [422], [511], [440], and [533]crystal planes is calculated to be 4.93, 2.99, 2.54, 2.11, 1.72, 1.62, 1.48, and 1.28 Å, respectively. The first two are near to the measured values for the single-crystal HRTEM characterization in Figure 3d, and the latter seven are very near to those for standard Fe_3O_4: 2.966, 2.53, 2.096, 1.712, 1.614, 1.483, and 1.279 Å.[41] Although small traces of maghemite or hematite cannot be totally ruled out by the XRD, SAED, or HRTEM characterization, these results identify that the iron oxide NPs are mostly of the magnetite cubic spinel phase. The size, calculated by the Sherra equation[42] from the identified XRD peaks, is 9.4 ± 2.4 nm, almost the same as that observed from the TEM images.

The long-term stability of the aqueous Fe_3O_4 NPs was also investigated. Results suggest that they can remain well dispersed in aqueous solution, as shown in Figure 3(a), even after being stored at room temperature for several months, evidenced by very little change in their dynamic diameters of around 38.0 ± 5.7 nm and in their Zeta potentials of about -32.6 ± 6.7 mV measured by dynamic light scattering (DLS) and Zeta-potential analysis (BIC DB-525, USA) before and after storage at room temperature for more than three months. The real diameters of those NPs after storing for three months are around 10.2 ± 3.0 nm determined by TEM images, which is almost the same as those initially prepared. The larger dynamic diameters than the real diameters obtained by TEM is a result of the formation of NP aggregates in aqueous solution, which is very common for NP solutions. The excellent aqueous stability is probably due to the synergistic effect of the three stabilizers.

Magnetic measurements of these ultrasmall NPs were conducted, and the room-temperature magnetization data is shown in Figure 4. The hysteresis loop shows that for these Fe_3O_4 NPs the saturation magnetization is 48.0 emu/g with an applied magnetic field of 5000 Oe (0.5 T), and there is a very small coercivity (< 30 Oe) at room temperature (Figure 5). The nonzero coercivity is probably caused by the aggregation of the NPs during precipitation, drying, and sample preparation, which may result in a fraction of large ferromagnetic particles. Generally, the results indicate that these NPs show excellent superparamagnetism with a low saturation field and a high susceptibility if well dispersed in aqueous solution, which are very promising characteristics for NPs to be used as MRI contrast agents with a rapid response at low magnetic fields.

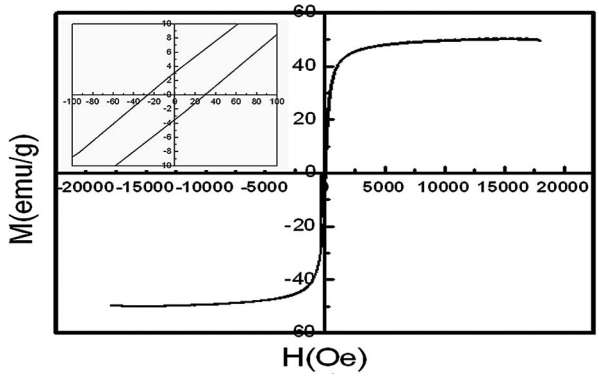

Figure 5. Hysterisis loop of the Fe_3O_4 NPs at room temperature.

In the development of new magnetic contrast agents for the clinical diagnosis of diseases, the contrast enhancing effects, biosafety, and metabolism of these magnetic nanoparticles in living tissue are preliminary issues in the determination of the optimized dosage and diagnosis time for high-contrast imaging in precisely discovering disease.[1] Although previous investigations have shown little toxicity and no significant side effects for Fe_3O_4 NPs as MRI contrast agents,[1–5,8,9,15,36] it is still important to investigate and understand the pathway, distribution, and metabolism time for these newly synthesized NPs in vivo, particularly for these aqueous-phase NPs stabilized by the surface coating of the three chemicals.

Here, the contrast-enhancing effects and the response time of these newly synthesized stable Fe_3O_4 NPs as MRI contrast agents to image the liver epithelial cells in the rabbit model are firstly examined in vivo. Results at the early stage after injection (the first half hour) are shown in Figure 6. Significant darkening of the liver epithelial cells can be observed within 26 min after injection, with T_2 reduced from 9.30 ± 0.89 ms to 7.52 ± 0.83 ms, which is about 20% reduction, indicating a much rapid in vivo response to these NPs by the liver of the model rabbit. Clearly, a significant liver signal loss can be observed after the Fe_3O_4 NP injection, and the course of uptake and clearance of iron in the liver can be observed by MRI.

In order to reveal the duration period with the optimized imaging contrast enhanced by these Fe_3O_4 NPs for the clinical manipulation, long-term observation (ca. 12 h) of the signal intensity of the MR images was conducted by imaging the live epithelial cells in the model rabbit's liver before and after injection of Fe_3O_4 NPs with a dosage of 15.2 mg Fe/kg rabbit. Each 2 h the MR images were re-

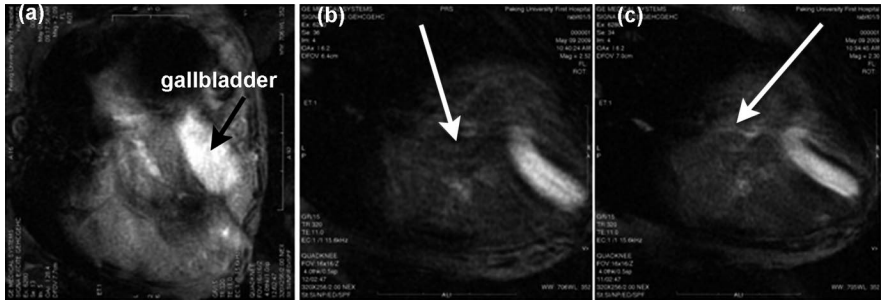

Figure 6. MR images of the rabbit liver before and after injection of Fe_3O_4 nanoprobes at a dosage of 0.68 mg Fe per kg rabbit at the early stage: (a) before injection, (b) 20 min after injection, (c) 26 min after injection. The results suggest that T_2 is reduced from 9.298 ± 0.893 ms to 7.517 ± 0.830 ms, approximately 20% reduction.

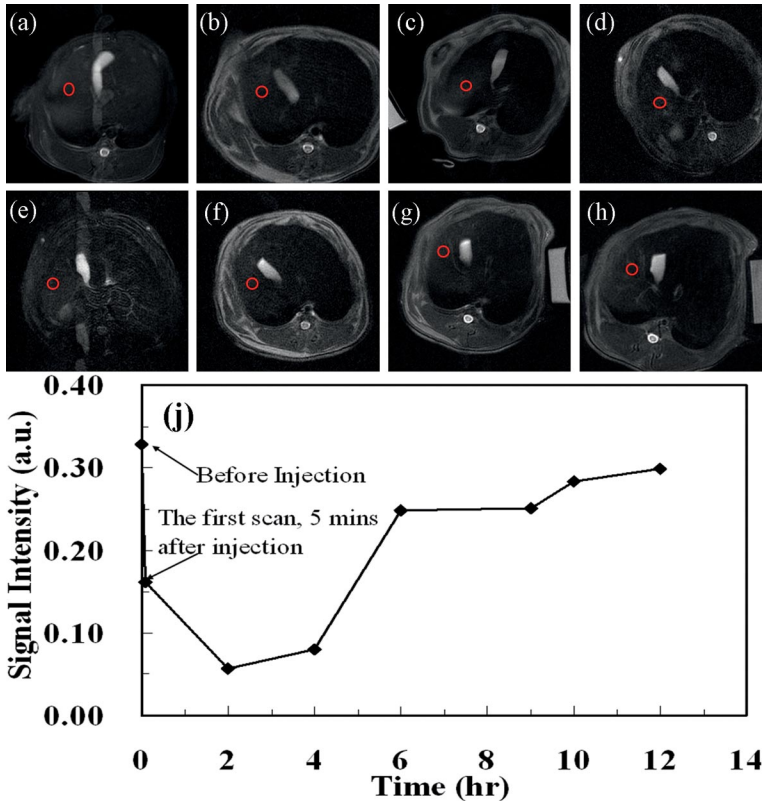

Figure 7. Long-term observation of contrasts in MR images of the rabbit liver at an injection dosage of 15.2 mg Fe per kg rabbit: (a) before injection of the Fe_3O_4 nanoprobes, (b) first scan at about 5 min after injection, (c) 2 h, (d) 4 h, (e) 6 h, (f) 8 h, (g) 10 h, (h) 12 h after injection. The relative signal intensity (SI; ratio of the signal of the liver and of normal saline) in T_2 weighted imaging (WI) [red circles in (a)–(h)]: SI liver/SI NPs of the liver after injection of Fe_3O_4 NPs changes continuously with time passed and is summarized in (j), showing the lowest point after injection.

corded and are shown in Figure 7(a)–(h); a normal saline solution was used as the standard signal intensity during image recording. A significant darkening of the liver epithelial cells was observed [Figure 7(a)–(h)] in the first 4 h. The time/signal curve was drawn to describe the signal change before and after Fe_3O_4 NP injection [Figure 7(j)] for the duration time of 12 h. The general trend of the changes is that the signal declines quickly and then elevates with the nadir at 2 h. Even in the first scan [Figure 7(j)], performed at around 5 min after injection (including the injection and handling time to transfer the rabbit to the machine), the relative liver signal intensity was reduced from 0.33 to 0.16 as 5 min is enough for several cycles of blood recycling in the rabbit. This result indicates that our Fe_3O_4 nanoprobes are very sensitive and have a good biocompatibility, and can be taken up by the liver rapidly to darken the targeting sites and increase the contrast of MR images. Then the signal is reduced to its minimum at 2 h after injection, suggesting that the uptake of Fe_3O_4 NPs by the liver reaches saturation. After the nadir, there is a relatively slow signal increase, suggesting that the Fe_3O_4 NPs are released from the liver by blood recycling. A relatively rapid increase between 4 h and 6 h occurs, meaning that the release of the Fe_3O_4 NPs becomes faster after an induction period. Finally, a normal signal level is approached slowly 12 h after injection. The shape of the curve of the signal changes is a quasi-inverted parabola. These findings demonstrate that the liver takes up the maximum amount of Fe_3O_4 NPs 2 h after injection. Thus, the time that the liver takes up the maximum concentration of Fe_3O_4 NPs can be determined as approximately 2 h after the Fe_3O_4 NP administration. The maximum amount of the Fe_3O_4 NPs the liver takes up will result in the lowest signal of the liver in the MR image [Figure 7(c)]. Although the liver begins to eliminate the NPs after 2 h, it is found that the release of the NPs from the liver experiences a slow process for the next 2 h [Figure 7(d)], and then a much rapid removal process in the following 2 h [Figure 7(e)–(h), Figure 7(j)]. The early two time points are crucial in clinical manipulation. It indicates that the optimized MR imaging of the liver can be obtained at 2 h after administration. At this time point, the imaging contrast is the best owing to the lowest signal intensity of normal liver background and relative highest signal intensity of any lesions. In addition, there are still at least two additional hours of clinical manipulation available to record the MR images at a high enough enhanced contrast after injection for 2 h. Four hours after injection, as the rapid clearance of the iron starts, the signal intensity of the liver is increased rapidly over the following 2 h.

Because the Fe_3O_4 NPs contain iron ions, its distribution in vivo may have a relationship with the metabolism of iron in the body. The distribution and duration of these NPs in different organs of the model rabbits were further tested for their metabolic behavior as a contrast agent. Liver, spleen, kidney (not shown in this article), and bone marrow tissues were isolated and evaluated 2 or 3 d after administration of the Fe_3O_4 NPs (Figure 8). The histopathological characteristics of these organs with hematoxylin–eosin staining were tested and analyzed. Positive results were found only in the spleen [arrowed in Figure 8(b)]. This result indicates that the Fe_3O_4 NPs do not show any weak toxicity to the organs tested and finally enter into the spleen without obvious retention in any related organs after recycling for 2 or 3 d.

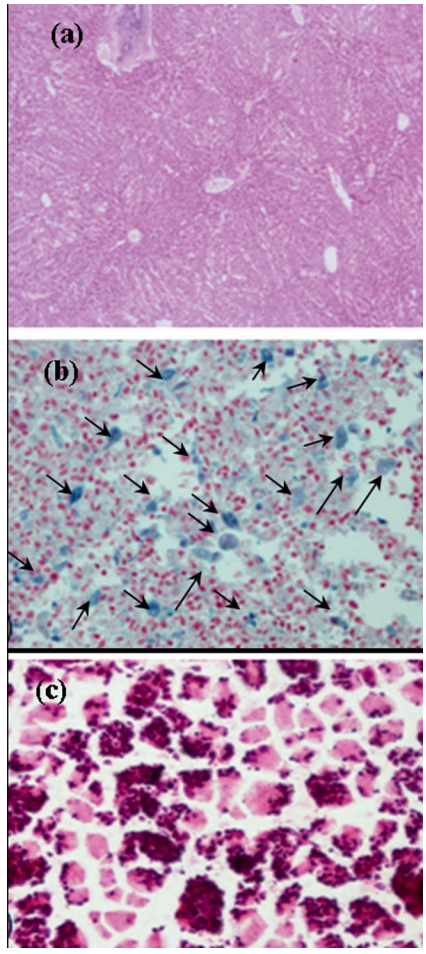

Figure 8. Results from the pathological analysis of tissue slices after Prussian blue dyeing: pathological slice of (a) liver, (b) spleen, (c) bone marrow.

When the iron is transferred into the spleen, it is important for iron recycling by splenic macrophages of the red pulp. Erythrophagocytosis is important for the turnover of erythrocytes, and recycling of iron is an important task for splenic macrophages, in conjunction with the liver. Iron that is not used or released by a cell is stored as ferritin, which is a cytosolic protein. For the storage of large amounts of iron in a cell, ferritin can aggregate into haemosiderin, which is an insoluble complex of partially degraded ferritin, deposits of which can be easily observed in red pulp macrophages [Figure 8(b)]. Erythrocytes are hydrolysed in the phagolysosome of macrophages, from which heme is released after the proteolytic degradation of hemoglobin. Heme is then further catabolized into biliverdin, carbon monoxide, and ferrous iron (Fe^{2+}), after which the iron is either released from the cells or stored. Although the white pulp is organized as lymphoid sheaths, with T- and B-cell compartments, around the branching arterial vessels, it

closely resembles the structure of a lymph node.[43,44] For the function of the spleen, it is well known that the red pulp of the spleen is responsible for iron recycling.[44] It is also known that iron recycling occurs intracellularly, and iron can be stored in the spleen for a long time. Hence, in our study, after 12 h, 24 h, and 3 d following administration of the Fe_3O_4 nanoparticles, the iron can be seen depositing in the splenic macrophages in the red pulp on the histopathological slice.

Conclusions

Ultrasmall, aqueous-phase, magnetite (Fe_3O_4) NPs, with a size of 9.8 ± 3.0 nm, have been successfully prepared by a modified iron salt coprecipitation process using PVP, TSC, and MAH as stabilizers. The synergistic effect from the combined stabilizers endows these NPs with good aqueous dispersion stability and excellent biocompatibility. These NPs have excellent superparamagnetic properties at room temperature, with a very low coercivity and a high saturation magnetization at low-saturation magnetic fields. They express significant enhancement in the MRI images of the liver epithelial cells in the living animal with an optimized clinical manipulation period for at least 2 h after injection and have no obvious toxicity for the organs examined in the animal model. As newly developed MRI contrast agents, they have the ability to target the liver epithelial reticular lymph nodes as evidenced in the in vivo study of liver cells in the rabbit models. This kind of magnetic nanoprobe could potentially be used as an MRI contrast agent for early diagnosing of lymphoma node metastasis and liver cancer.

Experimental Section

Synthesis of Stable Fe_3O_4 Nanoparticles: All chemicals were Analytical Reagent grade, purchased from the Beijing Chemical Reagent Co. Ltd., and used as received. The reactions were carried out under nitrogen with vigorous stirring. The process for preparing Fe_3O_4 NPs by controlled chemical coprecipitation is illustrated in Scheme 1. The PVP-dispersed iron salt solution was prepared by mixing PVP (10.0 g, 0.0033 mol), $FeCl_3{\cdot}6H_2O$ (0.676 g, 2.5 mmol), and $FeCl_2{\cdot}4H_2O$ (0.343 g, 1.73 mmol) in nanopure water (300 mL). The mixture was heated to 60 °C and stirred vigorously by sonication. NH_4OH solution (58 mL, 16 vol-%; concentration of original NH_4OH: 25%) was added dropwise and stirred vigorously for 30 min. To the resulting black solution was added dropwise a TSC solution (200 mL, 10.0 g, 34.0 mmol) over 30 min. MAH (50 mL, 0.3 g, 3.1 mmol) was then added dropwise over 20 min. After addition of the MAH solution, the mixture was heated to reflux for 2.5 h. The reaction was quenched with ice-cold water. The resulting black solution was centrifuged at 15000 rpm to permit the Fe_3O_4 NPs to settle out of the solution. The supernatant was decanted, and the same volume of nanopure water was added into the bottle, which was sonicated to form a uniform solution of NPs. This solution was centrifuged again at 15000 rpm, the supernatant was decanted again, and the black slurry was collected. Some of the slurry was dried at room temperature to obtain the Fe_3O_4 NPs as a black powder and the remainder of the slurry was redissolved in nanopure water and stored in a refrigerator for future use.

Composition and Structure Characterization of Magnetite Nanoparticles: The surface coatings of the Fe_3O_4 NP complexes (Fe_3O_4 coated by PVP, Fe_3O_4 coated by PVP and STC, Fe_3O_4 coated by PVP, STC, and MAH) were analyzed by FTIR (Thermo Nicolet nexus 670 spectrometer) to investigate the reason for the stability of the NPs, by comparison with the spectrum for the naked Fe_3O_4.[25,26,30] Thermogravimetric analysis (TGA, Q5000, TA instrument Inc., USA) was used to analyze the weight loss of the NPs at elevated temperatures as additional evidence of their surface coating by the three stabilizers. EDS was used to characterize the Fe/O ratio in the washed Fe_3O_4 NPs. The size, size distribution, and morphology of the NPs were examined by using HRTEM (JEOL-2010F) with a 200 kV field emission gun, coupled with an SAED device that was used to identify the crystal structure of the NPs. The NP solution was drop-cast onto a 200 mesh copper grid (Ager Scientific Ltd, UK), and the grid was air-dried at room temperature before being loaded into the microscope. XRD (RINT2000, Cu Target, 40 kV, 40 mA, λ = 1.54056 Å) was employed to confirm the crystal structure and the size of the Fe_3O_4 NPs. The magnetic properties of the Fe_3O_4 NPs were studied with a vibrating sample magnetometer (Lakeshore-7307, USA). The magnetization of the encapsulated particles vs. the applied field at room temperature (300 K) was measured with a maximum applied field of 20 kOe.

MR Imaging: MRI experiments were performed by using normal white rabbits weighing 3.0 kg. The experimental protocol was approved by the animal care committee at Peking University First Hospital. Animals were allowed food and water ad libitum. A solution of Fe_3O_4 NPs (10 mL, 6.3 mg/mL) was injected into a vein into a rabbit at a dosage of 15.2 mg Fe per kg rabbit with an intravenous injection of sodium phenobarbital (1.5 mL, 2%) for anesthesia at 0.5 mL per kilogram of body weight. Sequential MRI was performed every 2 h for 5–10 min after Fe_3O_4 NPs administration, to record the signal change of the liver, until the lowest signal point appeared. The MRI was performed at 0–12 h by using a 3.0 T magnetic resonance imager (3.0 T, Sigma, GE Medical Systems. Milwaukee, WI, USA) with a knee coil to improve resolution. After routine localization images were obtained, coronal and axial T_2-weighted spin-echo images were obtained (repetition time/echo time = 3400 ms/85.6 ms; echo train length = 18; section thickness = 3 mm; field of view = 18 cm; matrix, 320×256; number of signals acquired = 3). The total number of rabbits used was four, and one died during anesthesia.

Cytotoxicity and Metabolism Studies of NPs: 2 d after injection of the NPs, the rabbits were injected with a lethal dose (90 mg/kg body weight) of sodium pentobarbital. The liver, spleen, kidney, and bone marrow were isolated. The harvested organs for each rabbit were placed in individual trays for processing, and tray numbers were recorded. The dissected organs were fixed with 10% formalin. The organs were then embedded in paraffin and prepared sections (approximately 5 μm thick) taken at 0.5 mm intervals were stained with Prussian blue, and the bone marrow was stained with hematoxylin/eosin for microscopic examination by a pathologist. The pathologist examined the organs for the presence of iron in the cells, represented by a blue color in the slice.

Supporting Information (see footnote on the first page of this article): The measured FTIR spectra for the pure poly(vinlypyrrolidone) (PVP), trisodium citrate (TSC) and maleic anhydride (MAH) used in the experiments are presented.

Acknowledgments

The research was partially supported by the Peking University Biomed-X Foundation, the China International Science and Technology Cooperation (2008KR1330), the National Natural Science Foundation of China (10774009), the National Basic Research Program of China (2006CB910706), and The Fundamental Research Funds for the Central Universities in China. Y. S. appreciates financial support from the National Natural Science Foundation of China (NSFC) (50971010), the Basic Research Vision Funds (YWF-11-03-Q-002, Beihang University), the Scientific Research Foundation for the Returned Overseas Chinese Scholars, State Education Ministry (SRF for ROCS, SEM), New Teacher Funds (2008-00061025). Y. S. is also grateful to Professor Wantai Yang and Professor Lianying Liu at Beijing University of Chemical Technology for the use of the FTIR, DLS, and Zeta potential analyzer.

[1] E. X. Wu, H. Tang, J. H. Jensen, *NMR Biomed.* **2004**, *17*, 478–483.
[2] M. Memarsadeghi, C. C. Riedl, A. Kaneider, A. Galid, M. Rudas, W. Matzek, T. Helbich, *Radiology* **2006**, *241*, 367–377.
[3] C. A. Taschner, S. G. Wetzel, M. Tolnay, J. Froehlich, A. Merlo, E. W. Radue, *A Jr., Am. J. Roentgenol.* **2005**, *185*, 1477–1486.
[4] S. A. Schmitz, S. Winterhalter, S. Schiffler, R. Gust, S. Wagner, M. Kresse, S. E. Coupland, S. Wolfhard, *Radiology* **2001**, *221*, 237–243.
[5] Y.-w. Jun, J.-H. Lee, J. Cheon, *Angew. Chem. Int. Ed.* **2008**, *47*, 5122–5135.
[6] W. Wu, Q. He, C. Jiang, *Nanoscale Res. Lett.* **2008**, *3*, 397–415.
[7] Y.-w. Jun, J.-w. Seo, J. Cheon, *Acc. Chem. Res.* **2008**, *41*, 179–189.
[8] L. M. Lacava, Z. G. Lacava, M. F. Da Silva, O. Silva, S. B. Chaves, R. B. Azevedo, F. Pelegrini, C. Gansau, N. Buske, D. Sabolovic, *Biophys. J.* **2001**, *80*, 2483–2486.
[9] N. Kohler, C. Sun, A. Fichtenholtz, J. Gunn, C. Fang, M. Q. Zhang, *Small* **2006**, *2*, 785–792.
[10] H. Furusho, K. Kitano, S. Hamaguchi, Y. Nagasaki, *Chem. Mater.* **2009**, *21*, 3526–3535.
[11] T. Uchida, M. Wakakura, A. Miyake, T. Ogawa, *J. Therm. Anal. Calori.* **2008**, *93*, 47–52.
[12] N. R. Jana, Y. Chen, X. Peng, *Chem. Mater.* **2004**, *16*, 3931–3935.
[13] S. Sun, H. Zeng, D. B. Robinson, S. Raoux, P. M. Rice, S. X. Wang, G. Li, *J. Am. Chem. Soc.* **2004**, *126*, 273–279.
[14] Y. Hou, Z. Xu, S. Sun, *Angew. Chem. Int. Ed.* **2007**, *46*.
[15] T.-J. Chen, T.-H. Cheng, C.-Y. Chen, S. C. N. Hsu, T.-L. Cheng, G.-C. Liu, Y.-M. Wang, *J. Biol. Inorg. Chem.* **2009**, *14*, 253–260.
[16] U. Schwertmann, R. M. Cornell, (**1991**) *Iron Oxides in the Laboratory – Preparation and Characterization*, VCH Verlagsgesellschaft, Weinheim **1991**.
[17] S. Chen, J. Feng, X. Guo, J. Hong, W. Ding, *Mater. Lett.* **2005**, *59*, 985–988.
[18] D.-S. Baea, K.-S. Hana, S.-B. Choc, S.-H. Choib, *Mater. Lett.* **2007**, *37*, 255–258.
[19] Y. Song, P. Jin, T. Zhang, *Mater. Lett.* **2010**, *64*, 1789–1792.
[20] Y. Song, L. L. Henry, *Nanoscale Res. Lett.* **2009**, *4*, 1130–1134.
[21] G. S. Metraux, C. A. Mirkin, *Adv. Mater.* **2005**, *17*, 412–415.
[22] A.-h. Lu, E. L. Salabas, F. Schuth, *Angew. Chem. Int. Ed.* **2007**, *46*, 1222–1244.
[23] N. Arsalani, H. Fattahi, M. Nazarpoor, *Polym. Lett.* **2010**, *4*, 329–338.
[24] C. Y. Wang, J. M. Hong, G. Chen, Y. Zhang, N. Gu, *Chin. Chem. Lett.* **2010**, *21*, 179–182.
[25] R. Cornell, U. Schwertmann, *The Iron Oxide: Structure, Properties, Reactions, Occurrence and Uses*, Wiley-VCH, Weinheim, **1996**.
[26] M. Ma, Y. Zhang, W. Yu, H.-y. Shen, H.-q. Zhang, N. Gu, *Colloids Surf., A* **2003**, *212*, 219–226.
[27] X. Lu, M. Niu, R. Qiao, M. Gao, *J. Phys. Chem. B* **2008**, *112*, 14390–14394.
[28] Y. Song, F. Liu, B. Sun, *J. Appl. Polym. Sci.* **2005**, *95*, 1251–1256.
[29] Y. Song, C. Liu, *J. Appl. Polym. Sci.* **2006**, *101*, 3781–3792.
[30] L. T. Hoa, T. T. Dung, T. M. Danh, N. H. Duc, D. M. Chien, *J. Phys.: Conf. Ser.* **2009**, *187*, 012048.
[31] S.-S. Wei, Y.-F. Zhu, Y. Zhang, J. R. Xu, *React. Funct. Polym.* **2006**, *66*, 1272–1277.
[32] S.-Y. Zhao, D. K. Lee, C. W. Kim, H. G. Cha, Y. H. Kim, Y. S. Kang, *Bull. Korean Chem. Soc.* **2006**, *27*, 237–242.
[33] Y. Hou, H. Kondoh, M. Shimojo, E. O. Sako, N. Ozaki, T. Kogure, T. Ohta, *J. Phys. Chem. B* **2005**, *109*, 4845–4852.
[34] X.-F. Qu, Q.-Z. Yao, G.-T. Zhou, S.-Q. Fu, J.-L. Huang, *J. Phys. Chem. C* **2010**, *114*, 8734–8740.
[35] Y. K. Du, P. Yang, Z. G. Mou, N. P. Hua, L. Jiang, *J. Appl. Polym. Sci.* **2006**, *99*, 23–26.
[36] F. Xu, C. Cheng, F. Xu, C. Zhang, H. Xu, X. Xie, D. Yin, H. Gu, *Nanotechnology* **2009**, *20*, 405102-1-10.
[37] R. H. Grubbs, W. Tumas, *Science* **1989**, *243*, 907–915.
[38] T. Viswanathan, J. Jethmalani, *J. Chem. Educ.* **1993**, *70*, 165–166.
[39] N. Guan, Y. Wang, S. Dejun, J. Xu, *Nanotechnology* **2009**, *20*, 105603.
[40] M. Yamaura, R. L. Camilo, L. C. Sampaio, M. A. Macedo, M. Nakamura, H. E. Toma, *J. Magn. Magn. Mater.* **2004**, *279*, 210–217.
[41] J. Li, H. Zeng, S. Sun, J. P. Liu, Z. L. Wang, *J. Phys. Chem. B* **2004**, *108*, 14005–14008.
[42] B. D. Cullity, S. R. Stock, *Elements of X-ray Diffraction*, 3rd ed., Prentice Hall, Inc., Upper Saddle River, NJ, USA, **2001**, chapter 5 and appendix 5.
[43] J. E. Skandalakis, L. J. Skandalakis, P. N. Skandalakis, J. F. Sweeney, Spleen Introduction, *Anatomic Basis of Tumor Surgery*, **2010**, p. 603–635.
[44] Z. S. Khlystova, S. P. Shmeleva, O. P. Ryabchikov, N. A. Chuich, *Bull. Exp. Biol. Med.* **1981**, *92*, 1710–1713.

Received: January 7, 2011
Published Online: July 1, 2011

